HIGH RESOLUTION μ-CT COMBINED TO NUMERICAL MODELS TO ASSESS ELECTRICAL PROPERTIES OF BIMODAL CARBONATES

S. Youssef[1] , M. Han[1,2] , D. Bauer[1] , E. Rosenberg[1] , S. Bekri[1] , M. Fleury[1] , O. Vizika[1]

[1]*IFP, 1 et 4, avenue de Bois-Préau, 92852 Rueil-Malmaison Cedex, France*

[2]*Physique de la Matière Condensée, Ecole Polytechnique, CNRS 91128 Palaiseau, France*

This paper was prepared for presentation at the International Symposium of the Society of Core Analysts held in Abu Dhabi, UAE 29 October-2 November, 2008

ABSTRACT

The numerical simulation of petrophysical properties in complex carbonate rocks is a challenging task due to the unpredictable influence of the microporosity. This is particularly true for electrical properties (formation factor and resistivity index) for which both the amount and spatial distribution of microporosity plays a crucial role. We show a general methodology to simulate electrical properties using pore network models (PNM), starting from 3D μ-CT images. The simulations are performed on structures already studied by Random Walk (RW) techniques. With the available present technology, the micropore structure cannot be resolved but its spatial distribution within the macropore system can be identified. We show the importance of image acquisition and processing, a preliminary step before producing a three level porosity image comprising the solid, the microporosity and the resolved macropores. Then a macropore network model is built, in which the microporosity is randomly distributed along a defined fraction of throats, acting electrically in parallel. Then, formation factor and resistivity index are calculated and compared to experimental values in drainage. A study of the two main parameters introduced in the simulation allows an exploration of the electrical response. Archie behaviour as well as double curvature curves can be observed.

INTRODUCTION

Carbonate fields are expected to dominate production through the next years (over 50% of today world reserves) so it becomes a priority for industry to better understand carbonate behaviour. However evaluating reservoir using standard resistivity interpretation (Archie, 1942; Schlumberger, 1987) generally fails in carbonates which have complex pore structures (Dixon *et al.,* 1990). The cementation and saturation exponents (m and n) sometimes vary dramatically from the conventionally assumed value of 2 (Bouvier *et al.*, 1991; Fleury, 2002; Focke *et al.*, 1987). Understanding how rock properties depend on the pore structure is thus necessary for an optimal recovery strategy. Many research efforts have focussed on the relationship between the porous structure and the electrical properties using theoretical models such as effective medium and percolation theories (Sen, 1997; Zhou *et al.,* 1997) or numerical models based on 3D reconstructed image and stochastic network (Bekri *et al.,* 2003; Ioannidis *et al.*, 1997; Moctezuma-Berthier *et al.*, 2003). These models work well for rocks with a homogeneous matrix. The development of μ-CT facility gives the opportunity to go further in the complexity of rocks in terms of structure. In recent works, 3D images of the actual structure of bimodal carbonate rocks associated with the random walk technique (Han *et al.,* 2007) or finite element modelling (Knackstedt *et al.,* 2007) have been used to assess the electrical properties. These studies show the direct impact of the spatial distribution of the microporosity on the formation factor and the resistivity index.

The objective of the present work is to investigate the effect of pore architecture on electrical properties calculated with a dual-porosity pore network model used in drainage conditions. We carry out 3D μ-CT imaging, Pc, formation factor and resistivity index measurements during drainage on one sandstone and two carbonate rocks. We describe a methodology to assess microporosity properties from 3D images by three phase segmentation. Then we describe the use of a dual-pore network model taking into account both the actual resolved pore space and the spatial distribution of the microporous phase. Finally we present a parametric study to evaluate the impact of the local heterogeneity pattern of the microporous phase.

EXPERIMENTAL

Sample characterisation

Three samples are considered in this paper: clay free Fontainebleau sandstone and two bimodal pore size distribution carbonates (Estaillade limestone and Lavoux limestone). The experimental observations are summarized hereafter and the main petrophysical properties are reported in Table 1. For more details see (Fleury, 1998; Han *et al.*, 2008a; Han *et al.,* 2007).

***Fontainebleau sandstone**:* The key characteristic of this sample is the absence of clays at the quartz grain surface. Although some apparent flat surfaces can be observed, most of the grains present a slight surface roughness as seen in the SEM image (cf. Table 1). The sample has a strongly water-wet behavior. The RI - S_w curve measured in drainage on this Fontainebleau sample shows two different regimes of the resistivity: when the brine saturation is greater than about 20%, the data points follow a power law with an exponent n close to 2 which is in agreement with other measurements on clay free sandstones (Dunlap, 1949; Diederix, 1982). However, the bending down behavior at low S_w is rather unexpected and this new trend is rarely discussed in literature.

Estaillade limestone: This carbonate exhibits a bimodal pore size distribution (cf. mercury injection data in Table 1). It contains two types of pores: intergranular macro-pores, and intragranular micropores, found in some fossil grains called "red algae". We can also observe from the SEM image the presence of solid grains with diameters over 100 μm. The RI - S_w curve in drainage presents a non – Archie behavior. The curve shows a positive deviation when the saturation is below 40%.

***Lavoux limestone**:* This carbonate has also a bimodal pore size distribution, as shown by SEM images and the mercury injection (cf. Table 1). However, in this sample, the quantity of microporosity is more abundant, about 57% of total porosity and appears from visual observations on SEM images to be much better connected. The curve *RI* - S_w follows almost perfectly the Archie's law with an exponent value nearby 1.9.

Fontainebleau Sandstone	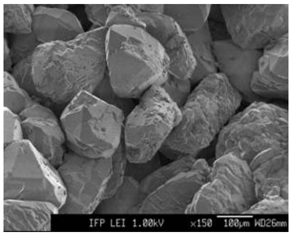 φ = 22 % FF = 11.5 K = 2100 md	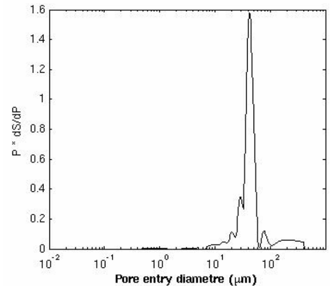	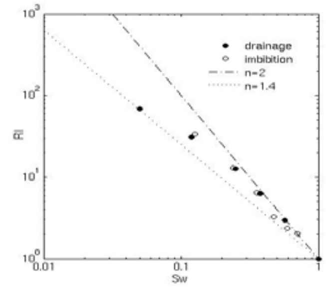
Estaillade limestone	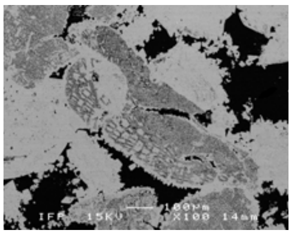 φ = 24.7% FF = 24, K = 273 md	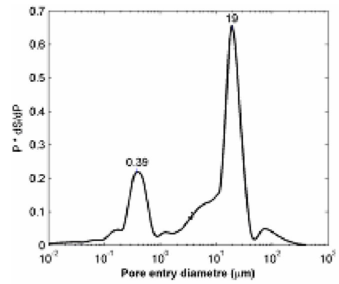	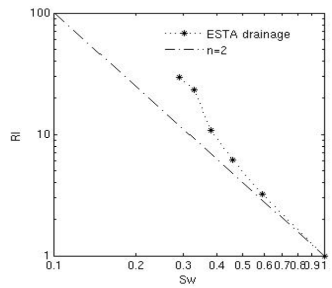
Lavoux limestone	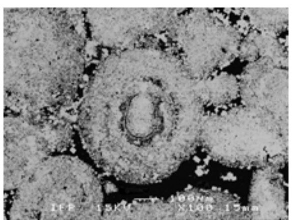 φ = 28.7 % FF = 13 K = 90 md	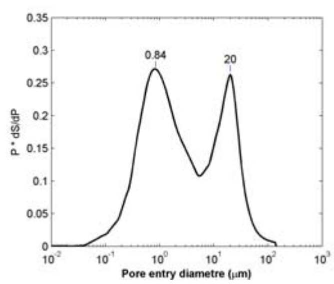	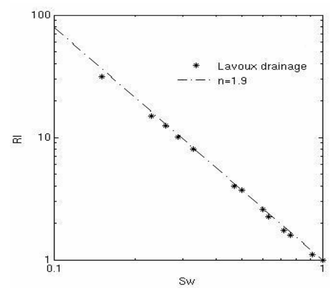
	SEM image and main petrophysical properties	***The mercury injection data***	***RI vs Sw curve***

Table 1: Experimental characterisation of samples studied.

<u>*Imaging setup*</u>

The μ-CT equipment installed at IFP is a Nanotom from PHOENIX X-Ray (Germany). The source is generated by the impact of a focussed electron beam on a thin target. Spot size varies between 1 and 5 microns depending on the operating conditions. Common acquisition parameters for rock analysis were the following: 5mm diameter sample, pixel size 3 μm, 2300×2300 field of view (more details can be found in (Youssef *et al.*, 2007)).

In order to optimize 3D image contrast a sample of Estaillade limestone was imaged with three different set-up conditions. Table 2 shows the resulting images (2D slice of 1000x1000 voxels) and the corresponding gray level histograms for different number of projections (1800 and 3600) and different filters (Cu and Al). It is clearly observed that increasing the number of projections reduces drastically the noise and enhances the image contrast for a given filter without any counterpart except a longer acquisition time.

Oppositely, the use of an Aluminum filter enhances the contrast but this gain is counterbalanced by the outbreak of ring artifacts which are present but do not deteriorate the image quality with the Cu filter. Following these observations, we chose for further acquisitions a number of projections of 3600 and a 0.1 mm thick Cu filter.

1800 projections	3600 projections	3600 projections
filter: Cu 0.1 mm	filter: Cu 0.1 mm	filter: Al 0.25 mm
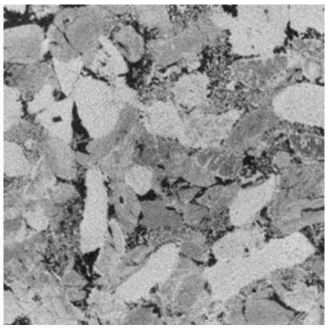	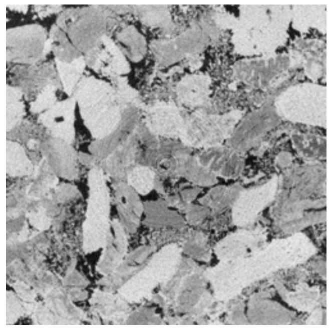	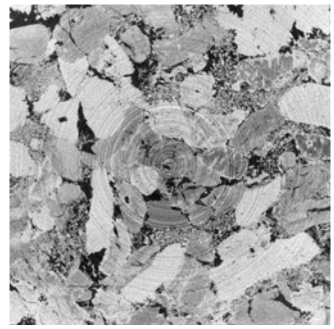
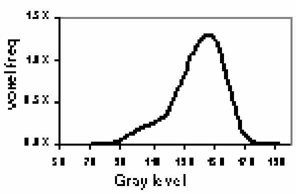	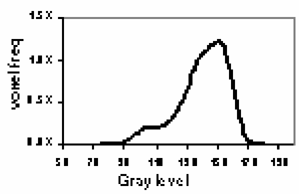	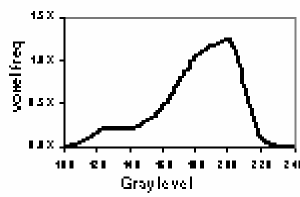

Table 2: 2D slices and gray level histograms of Estaillade for different X-ray CT set-ups.

IMAGE PROCESSING AND DATA EXTRACTION

Sample imaging

Samples described previously were imaged according to the optimal set-up previously defined. For the carbonate samples two adjacent regions of interest were imaged. For each scan a volume of 1000x1000x1000 voxels was reconstructed and converted in an 8bit gray level image. Figure 1 shows slices extracted from the reconstructed volumes. We can distinguish for the two carbonates a resolved macroporosity (pore size> 3μm), a microporouse phase (pore size<3μm) and a solid phase (compact bright grains).

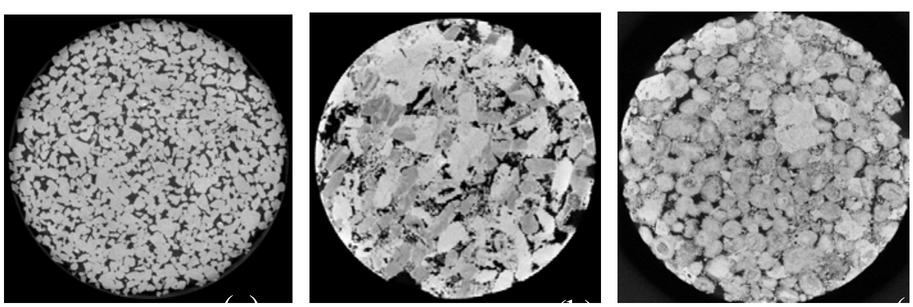

Figure 1: X-Ray density maps of Fontainebleau sandstone (a), Estaillade (b) and Lavoux lilmestone (c) samples extracted from 2000^3 voxel volumes at 3 μm resolution.

Three phase segmentation

The three phase segmentation process intends to separate correctly the solid dense phase, the macropores and the microporous phase. Note that, in this image treatment, the limit between micro and macropores is given by the μ-CT image resolution (3 microns). Even with the optimal μ-CT set-up raw images are still noisy (cf. Figure 2.a) and their gray level histograms are smooth. In order to separate the gray levels corresponding to each phase (macroporosity, microporosity and solid) the images have to be filtered. The filtered images are obtained by affecting to each voxel the average gray value of its 5^3 neighbors one (cf. Figure 2.b). This filter was found to be a good compromise between denoising and smoothing effect (the preliminary study was not reported here). As a consequence the contrast was enhanced and we get a better separation of the gray level peaks in the histograms (cf. figure 2.e). Following this operation one can distinguish three different peaks corresponding to the different phases. At this step we can evaluate the global porosity on each image. As the carbonate samples have a monomineral matrix, image porosity can be expressed as: $\phi_{img} = (g_s - g_m) / (g_s - g_v)$ where g_m is the mean gray level of the image and g_v and g_s are respectively the peaks' gray levels of void and the solid phase. The porosity estimation from images is in good agreement with the experimental ones with slight variations due to local heterogeneity (cf. Table 3).

By applying thresholds th1 and th2, a new composite image of the 3D phase distribution can be obtained (cf. figure 2.c). The resulting image still contains some artifacts due to phase transition between the void space and the solid phase (the gray level of the border have the same value as the microporous phase). This artifact is corrected by morphological operations (growing, shrinking and smoothing) which are equivalent to an isotropic dilatation (Caty *et al.*, 2008) as shown by Figure 2.d.

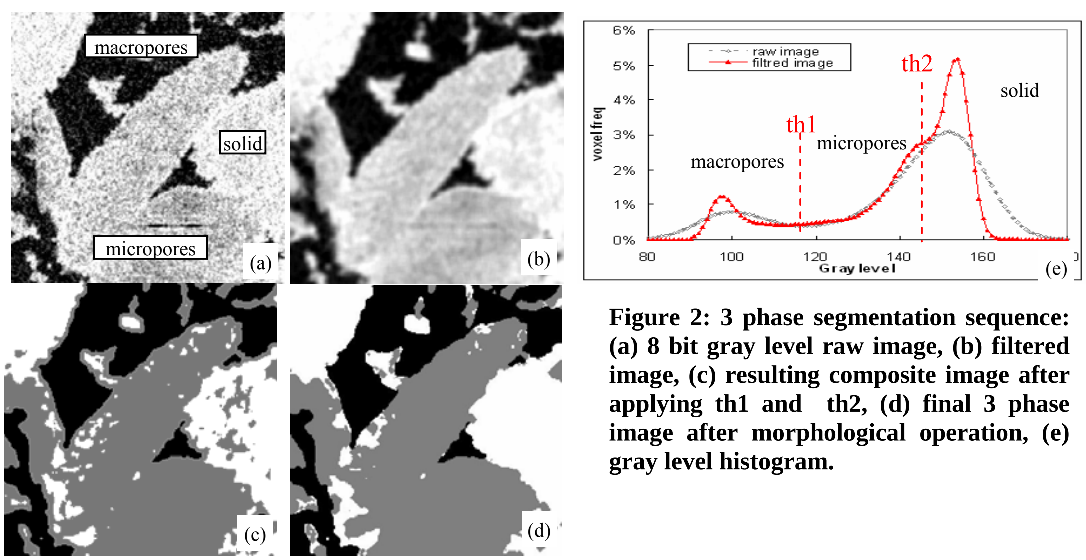

Figure 2: 3 phase segmentation sequence: (a) 8 bit gray level raw image, (b) filtered image, (c) resulting composite image after applying th1 and th2, (d) final 3 phase image after morphological operation, (e) gray level histogram.

Information extracted for simulations

The different phase fractions extracted from the composite image (reported in Table 3) can be expressed as $F_{ma}= N_{ma}/N_{img}$ and $F_{mi} = N_{mi} /N_{img}$ where F_{ma}, F_{mi}, N_{ma}, N_{mi} and N_{img} are respectively the resolved porosity fraction, the microporous phase fraction, the number of voxel of the resolved porosity, the number of voxel of the microporous phase and the total number of voxels in the image. The mean porosity (ϕ_{mi}) of the microporous phase can then be deduced from: $\phi_{mi} = (\phi_{img} - F_{ma}) / F_{mi}$. It is to be not that the resolved porosity in all samples is totally connected.

Another important parameter that can be accessed at this stage is the fraction of the macropore surface in contact with the microporous phase (F_{Surf}). To achieve this, triangulated surfaces representing the boundaries between the different phases are generated from the composite image (cf. Figure 3). The creation of surfaces with correct topology and optimized triangular shape from the segmented tomographic data is carried out automatically with the help of the marching cubes algorithm (Youssef *et al.*, 2005). Finally, the macropore phase can be isolated to build the corresponding equivalent pore network according to the methodology described in (Youssef *et al.*, 2007).

sample Id	ϕ_{exp} (%)	ϕ_{img} (%)	F_{ma} (%)	F_{mi} (%)	ϕ_{mi} (%)	F_{surf} (%)
GdF	22.0	21.6	21.5	#	#	#
EST 1	24.7	25.7	15.3	28.6	36	47
EST 2		23.5	13.9	28.3	34	34
LAV 1	28.7	28	8.6	66.7	29	81
LAV 2		29.8	11.6	62.7	28	78

Table 3: Quantification of samples porosities and phase fraction from 3D images: image porosity (ϕ_{img}), macropore fraction (F_{ma}), microporous phase fraction (F_{mi}), porosity of the microphase (ϕ_{mi}) and the fraction of the macropore surface in contact with the microporous phase (F_{surf})

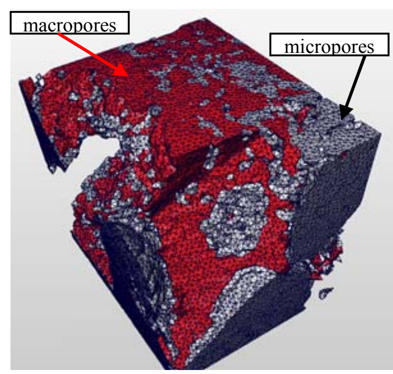

Figure 3: Surface model representing macro and micro phases from the Estaillade sample.

PORE NETWORK MODELING

Network invasion methodology

The capillary pressure saturation curve is obtained by simulating a quasi-static displacement. We consider a network of variable elements, i.e. a spatial distribution of nodes *i*, the pores, and bonds *ij* connecting the nodes *i* and *j*, the throats, where the conductance g_{ij} is located. Throat cross sections are supposed to be triangular whereas the nodes have a cubic shape. By applying a macroscopic pressure gradient across the whole network, fluid pressure P_{ij} in pores i and a flow rate q_{ij} in the throats can be calculated. Expressions to evaluate the saturations in each unit element can be found in (Laroche *et al.*, 2005).

Formation factor and resistivity index calculation

The electrical conductance of the water phase in a pore segment is given by $g_e = \sigma_w A_w / l$ where A_w represents the cross-sectional area occupied by the water phase, l the segment length and σ_w the electrical conductivity of bulk water. The calculation of the effective conductance between two neighbouring pores, takes into account the water phase occupancy in the different pore segments (pores and throats). The electrical current I_{ij} in each segment becomes then $I_{ij}= g_{ij} (U_i - U_j)$, where U_i and U_j stand for the electrical potential in the neighbouring pores i and j.

Dual porosity structure

The dual network model combines transport properties of the microporosity with the single pore network modelling approach used to simulate the interconnected macroporosity network. Both porosity types are supposed to act electrically and hydrodynamically in parallel. This means, we consider two parallel networks, connected in the nodes, where the fluid exchange takes place. The first one corresponds to the macropores, whereas the second one represents the macroscopic transport properties of the microporous phase (see Fig. 4). More details on the governing equations can be found in (Bekri *et al.*, 2005; Moctezuma-Berthier *et al.*, 2003). In the present work, pore-throat radii larger than the μ-CT resolution are used to build a three-dimensional entirely connected network of pores and throats representing the behavior of the macroporosity. Pores smaller than the μ-CT resolution are supposed to belong to the microporosity. Considering this fact, the capillary pressure P_c necessary to invade the microporous phase is always higher than the one required for the invasion of the macropores. Thus, during drainage, the non-wetting phase passes from the macropores to the microporous phase.

The volume of the microporosity acting in parallel to the macro pore segments is supposed to be the same for each segment. It is given by $V_{seg} = F_{mi} V_{img} / N_{seg} = A_{con} l_{con}$ where N_{seg} is the number of segments and V_{img} the volume of the 3D images ($F_{mi} V_{im}$ corresponds to the entire volume of the microporous phase). Supposing that the microporosity volume has a cuboid shape, we define A_{con} as the cross-section of the cuboid perpendicular to the flow direction, whereas l_{con} corresponds to its length parallel to the flow direction.

The electrical conductance of the microporous phase $g_{e,mi} (S_{w,mi} (P_c))$, depending on the water saturation of the microporous phase, is then given by:

$$g_{e,mi}(S_{w,mi}(P_c)) = \sigma_w [FF_{mi} RI_{mi}(S_{w,mi}(P_c))]^{-1} A_{con} / l_{con}$$

with $FF_{mi} = a\phi_{mi}^{-m,mi}$ and $RI_{mi}(S_{w,mi}(P_c)) = S_{w,mi}^{-n_{mi}}(P_c)$ where n_{mi} stands for the matrix saturation exponent and m_{mi} for the matrix cementation exponent. As can be seen, the ratio A_{con} / l_{con} strongly influences the conductance of the microporous phase.

Parameter determination

In order to perform physically realistic simulations using the dual porosity model, first of all, model parameters have to be determined using either experimental or numerical results or data from the μ-CT.

As described above the macropores are partially surrounded by a microporous phase. The contact surface F_{Surf} given in Table 3 is now transformed in a discrete number of macro pore segments whose microporosity conductivity is given by $g_{e,mi.}$ For the remaining pore segments $g_{e,mi.}$ is set equal to zero, representing the solid phase (cf. Figure 4). Pore segments with microporosity acting in parallel are randomly chosen. The percentage p_{seg} of these pore segments is then varied taking into account that the total volume of microporosity is constant. For instance, V_{seg} becomes then $V_{seg} = F_{mi}\ V_{img}\ /p_{seg}\ \ N_{seg}$. Additionally, the ratio A_{con}/l_{con} has been varied. The porosity of the microporous phase is deduced from the μ-CT measurement. If we assume that the microporosity is mainly a pack of calcite micrite, the cementation exponent m_{mi} can be set to m_{mi} = 1.5 (Bryant *et al.,* 1996; Sen *et al.,* 1981). In this work, we are mainly interested in the influence of the geometry of the microporous phase on the electrical transport properties. The influence of its petrophysical properties will be studied thoroughly in a future work. The oil/water capillary pressure of the microporous phase $P_{c,oil/water,mi}$ was calculated from the mercury injection curve assuming that all pores smaller than the μ-CT resolution belong to the microporous phase. The microporous phase saturation exponent was set to $n_{mi} = 2$ corresponding to the commonly used Archie exponent.

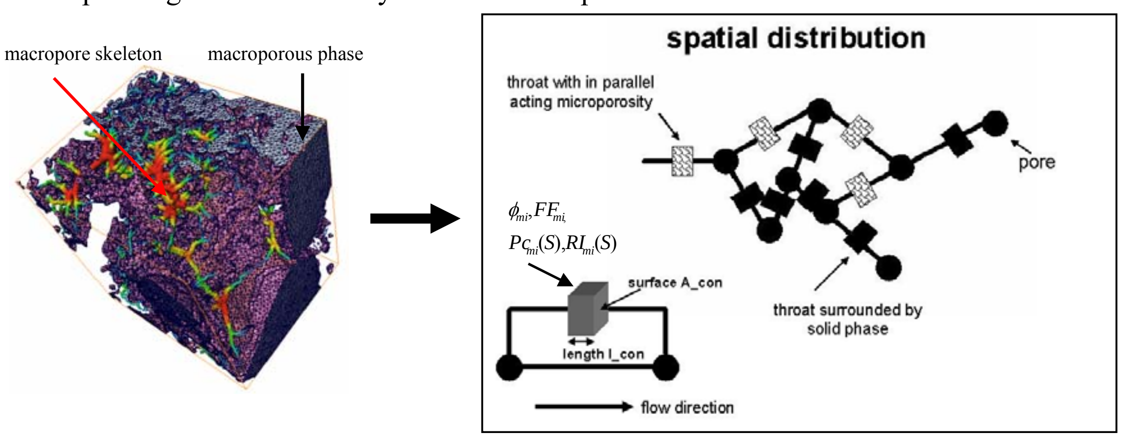

Figure 4: Description of the matrix surrounding the throats corresponding to the macroporosity (Left: Macropores surrounded by either microporous or solid phase, Right: Corresponding microporosity distribution in the PNM)

RESULTS

In a first step we compare experimental results (FF and RI) of a monomodal porous medium (Fontainebleau sandstone) with the numerical results of the random walk method (RW) and the single pore network model (PNM). Then, the dual network approach is applied to an Estaillades and a Lavoux carbonate.

Monomodal pore structure

Table 4 shows the experimental and numerical results of the FF. Numerical values obtained by PNM and RW are slightly higher than the experimentally observed ones, which is probably due to the heterogeneity of the sample. Figure 5 shows the resistivity index computed by the random walk technique (Han *et al.* 2008a) and by PNM, as well as the experimental results. The saturation exponent decreases from 2 at high water saturation, to about 1.5 at low water saturations. (Han *et al.* 2008a) have shown that this bending down deviation is due to the wetting phase film conductance. In the present situation, the introduction of film conductance in both RW and PNM simulations (where the film size of the PNM depends on the local pore pressure) is critical for reproducing the experimentally observed bending down deviation. Film conductance can be studied in details using RW techniques, as discussed in greater details in (Han *et al.* 2008b). Moreover, considering the fact that the RW technique is directly applied to the images without any assumptions on the pore structure, the good agreement between the RW results and the experiments indicate that the image acquisition and processing is valid.

PNM			***RW***	**Exp *FF***
FF_x	FF_y	FF_z	12.9	11.5±0.9
13.16	12.51	13.74		

Table 4: FF of Fontainebleau sandston

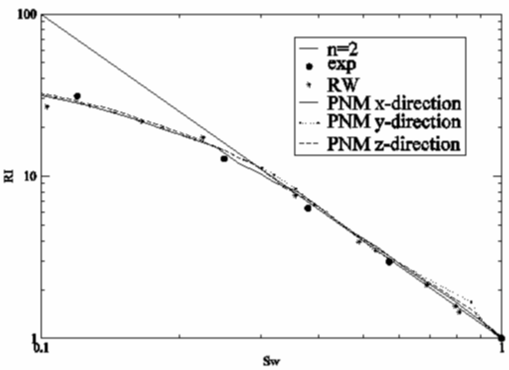

Figure 5: RI curve of Fontainebleau sandstone

Bimodal pore structure

As mentioned above two different carbonates (Estaillades and Lavoux), both presenting a very specific pore structure, were investigated. The main objective of this section is to investigate the influence of the spatial distribution of the microporous and the solid phase on the macroscopic transport properties.

Estaillades carbonate: Figure 6.a shows the results of the FF calculation as a function of the percentage of throats surrounded by microporosity p_{seg}. The calculations were done for $l_{con} = V_{seg}^{1/3} = 56.25\mu m$ assuming that the microporosity volume has a cubic structure and for $l_{con,i} = l_{ff,i}$ ($<l_{ff,i}>=11.04\mu m$) where $l_{ff,i}$ stands for the equivalent electrical length of a throat which is computed in the same manner that the equivalent throat length described in (Youssef *et al.,* 2007) considering the equivalent electrical conductivity of the throat. The resulting formation factors are relatively close to the experimental values. However, they are too high using $l_{con} = V_{seg}^{1/3}$ and too low for $l_{con,i} = l_{ff,i}$. This means that by correctly adapting the conductivity length of the microporosity l_{con}, the experimental value can be obtained. All values decrease with increasing p_{seg} as the number of percolating paths of microporosity volumes and therefore the overall conductivity of the microporosity increases.

Figure 6.b shows the RI values as a function of p_{seg}. Calculations were done with $l_{con} = V_{seg}^{1/3}$. RI values increasing with the decreasing p_{seg} . For $p_{seg} < 0.56$ the formation of

a double curvature can be seen. The double curvature can be explained as follows. For high wetting phase saturations ($S_w \geq 0.4$) a percolating path still exists in the wetting phase (into macropores or into the microporous phase). For intermediate wetting phase saturations ($0.3 < S_w < 0.4$), the percolation of the wetting phase is either provided by the microporous phase ($p_{seg} < 0.56$) or by the remaining water films lining the macropores ($p_{seg} \geq 0.56$). In the first case, the change in RI for a given change in wetting phase saturation ($\partial RI / \partial S_w$) is given by the electrical properties of the microporous phase. In the second case, the important change in the RI curvature corresponding to ($p_{seg} \geq 0.56$) results from the fact that there is no percolating path in the microporosity and the resistivity is dominated by the remaining water film. As it can be seen in Figure 6.b the numerical results for $p_{seg} = 0.56$ are in relatively good accordance with the experimental results (black dots). Additionally, we can state that $p_{seg} = 0.56$ is relatively close to the contact surface F_{Surf} obtained by the three phase segmentation (F_{Surf}=47%, see Table 3).

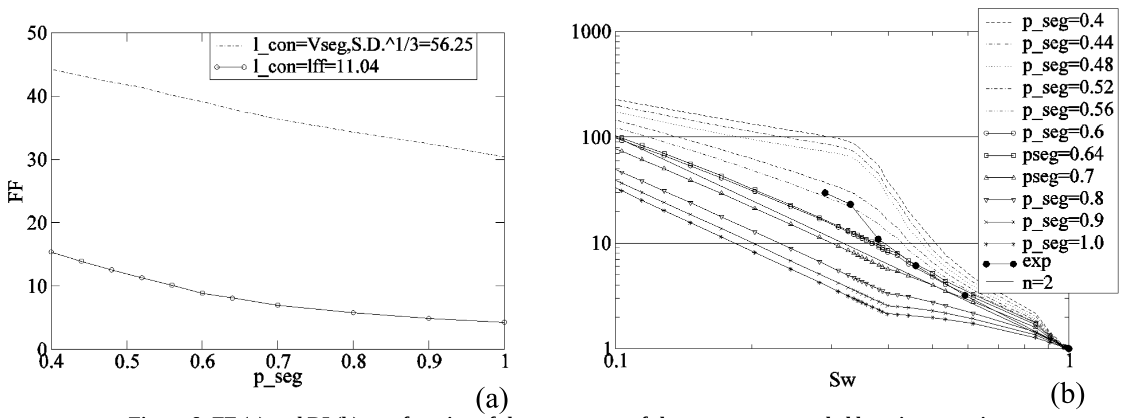

Figure 6: FF (a) and RI (b) as a function of the percentage of throats p_{seg} surrounded by microporosity

Lavoux carbonate: As shown before, the volume of the microporous phase of the Lavoux is much higher than the one of the Estaillades. Whereas the Estaillades requires a thorough investigation of p_{seg}, the conductivity length l_{con} of the microporous volume has more importance for the Lavoux carbonate. Thus, in the following l_{con} was varied and p_{seg} fixed to 0.78 (see Table 3). The experimentally observed saturation exponent value of the Lavoux is almost equal to 2 for the entire range of saturation. Figure 7 shows the FF and RI values for different conductivity length l_{con}. As can be seen, by correctly adapting l_{con} the RI values correspond well to the experimental results. However, considering the FF, we can state that all values shown in Figure 7 are higher than the experimental value (Table 1). This fact could probably be explained by the uncertainties in the assignment of electrical conductances to pores and throats, but also by the heterogeneity of the sample.

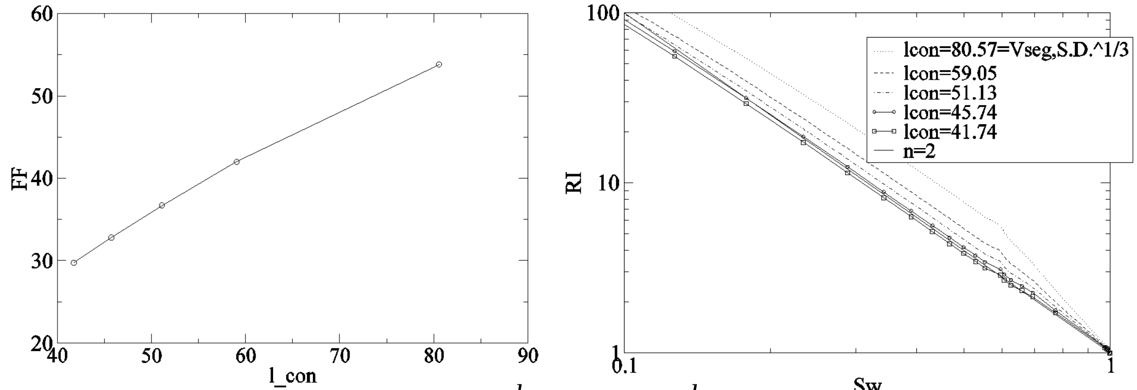

Figure 7: FF and RI as a function of l_{con} for pseg=0.78. l_{con} is given in microns.

CONCLUSION

We present a general methodology to reproduce the electrical responses of bimodal carbonate structures using pore network models. First, the simulations depend strongly on the image acquisition and processing for the identification of the microporosity. We propose an optimized processing to remove artefacts from high resolution μ-CT and extract important information such as the amount of macropore surface in contact with the microporous phase. In the pore network, the microporosity is modeled as a parallel circuit located along the macropore throats and characterized by a conductivity length l_{con}. A second parameter that can be varied in the network simulation is the number of throats (segments) p_{seg} in which microporosity is present. These two parameters have a different influence on the resistivity index curve. When the amount of microporosity is low, p_{seg} effect is important, and when the amount of microporsity is large, l_{con} effect is important.

REFERENCES

1. Archie, G.E.: "The electrical resistivity log as an aid in determining some reservoir characteristics," *Petroleum Transaction of the AIME* (1942), 146, 54-62.
2. Bekri, S., J. Howard, J. Muller, and P.M. Adler: "Electrical resistivity index in multiphase flow through porous media," *Transport in Porous Media* (2003), 51, 41-65.
3. Bekri, S., C. Laroche, and O. Vizika: "Pore network models to calculate transport and electrical properties of single or dual-prosity rocks", *Int. Sym. of the Society of Core Analysts*, Toronto, Canada (2005) .
4. Bouvier, L. and S. Maquignon: "Reconciliation of log and laboratory derived irreductible water saturation in double prosity reservoir," *Advances in Core Evaluation II: Reservoir Appraisal* (1991)
5. Bryant, S. and N. Pallatt: "Predicting formation factor and resistivity index in simple sandstones," *Journal of Petroleum Science and Engineering* (1996), 15, 169-179.
6. Caty, O., E. Maire, S. Youssef, and R. Buchet: "Modeling the properties of closed cell cellular materials from tomography images using finite shell elements," *submitted to Acta Materialia* (2008).

7. Dixon, J.R. and B.F. Marek: "The Effect of Bimodal- Pore Size Distribution on Electrical Properties of Some Middle Eastern Limestones", *SPE/ATCE*, New Orleans, Louisiana (1990) .
8. Fleury, M.: "Resistivity in Carbonates: New Insights", *SPE/ATCE*, San Antonio, Texas (2002) .
9. Fleury, M.: "FRIM: A fast resistivity index mesurment method", *Int. Sym. of the Society of Core Analysts*, The Hague, The Netherlands (1998).
10. Focke, J.W. and D. Munn: "Cementation Exponents in Middle Eastern Carbonate Reservoirs," *SPE Formation Evaluation* (1987), 2, 155-167.
11. Han, M., M. Fleury, and P. Levitz: "Effect of the pore structure on resistivity index curves", *Int. Sym. of the Society of Core Analysts*, Calgary, Canada (2007).
12. Han, M. et al.: "The effect of the porous structure on resistivity index curves. An experimental and numerical study", *SPWLA 49th Annual Logging Symposium*, Edinburgh, Scotland (2008a).
13. Han, M., S. Youssef, E. Rosenberg, M. Fleury, and P. Levitz: "Deviation from Archie law in partially saturated porous media: wetting films versus depercolation, in preparation," *in preparation* (2008b).
14. Ioannidis, M.A., M.J. Kwiecien, and I. Chatzis: "Electrical conductivity and percolation aspects of statistically homogeneous porous media," *Transport in Porous Media* (1997), 29, 61-83.
15. Knackstedt, M.A. et al.: "Pore scale analysis of electrical resistivity in complex core material", *Int. Sym. of the Society of Core Analysts*, Calgary, Canada (2007).
16. Laroche, C. and O. Vizika: "Two-phase flow properties prediction from small-scale data using pore-network modeling," *Transport in Porous Media* (2005), 61, 77-91.
17. Moctezuma-Berthier, A. et al.: "A dual network model for relative permeability of bimodal rocks: application in a vuggy carbonate", *Int. Sym. of the Society of Core Analysts*, Pau, France (2003).
18. Schlumberger, I.: "Log interpretation: Principles/Application," *Schlumberger Educational Services* (1987).
19. Sen, P.N.: "Resistivity of partially saturated carbonate rocks with microporosity," *Geophysics* (1997), 62, 415-425.
20. Sen, P.N., C. Scala, and M.H. Cohen: "A self-similar model for sedimentary rocks with application to the dielectric constant of fused glass beads," *Geophysics* (1981), 46, 781-795.
21. Youssef, S., E. Maire, and R. Gaertner: "Finite element modelling of the actual structure of cellular materials determined by X-ray tomography," *Acta Materialia* (2005), 53, 719-730.
22. Youssef, S. et al.: "Quantitative 3D characterisation of the pore space of real rocks : improved μ-CT resolution and pore extraction methodology", *Int. Sym. of the Society of Core Analysts*, Calgary, Canada (2007) .
23. Zhou, D.G., S. Arbabi, and E.H. Stenby: "A percolation study of wettability effect on the electrical properties of reservoir rocks," *Transport in Porous Media* (1997), 29, 85-98.